Gianluca Cusatis[1]
Assistant Professor
CEE Department,
Rensselaer Polytechnic Institute,
110 8th Street,
Troy, NY 12180
e-mail: cusatg@rpi.edu

Alessandro Beghini
Engineer
Owings and Merrill LLP,
224 South Michigan Avenue,
Chicago, IL 60604
e-mail: alessandro.beghini@som.com

Zdeněk P. Bažant[2]
Walter P. Murphy Professor and
McCormick School Professor
of Civil Engineering and Materials Science,
CEE Department,
Northwestern University,
2145 Sheridan Road,
Evanston, IL, 60208
e-mail: z-bazant@northwestern.edu

Spectral Stiffness Microplane Model for Quasibrittle Composite Laminates—Part I: Theory

The paper presents the spectral stiffness microplane model, which is a general constitutive model for unidirectional composite laminates, able to simulate the orthotropic stiffness, prepeak nonlinearity, failure envelopes, and, in tandem with the material characteristic length, also the post-peak softening and fracture. The framework of the microplane model is adopted. The model exploits the spectral decomposition of the transversely isotropic stiffness matrix of the material to define orthogonal strain modes at the microplane level. This decomposition is a generalization of the volumetric-deviatoric split already used by Bažant and co-workers in microplane models for concrete, steel, rocks, soils, and stiff foams. Linear strain-dependent yield limits (boundaries) are used to provide bounds for the normal and tangential microplane stresses, separately for each mode. A simple version, with an independent boundary for each mode, can capture the salient aspects of the response of a unidirectional laminate, although a version with limited mode coupling can fit the test data slightly better. The calibration of model parameters, verification by test data, and analysis of multidirectional laminates are postponed for the subsequent companion paper. [DOI: 10.1115/1.2744036]

Keywords: fiber composites, laminates, spectral methods, microplane model, fracture energy, crack band model, damage, failure criteria, finite elements

Dedicated to Professor Franz Ziegler of the Technical University of Vienna at the occasion of his 70th birthday.

Introduction

At an early stage of development of any field of science, different models exist for different situations. Such models have, of course, narrow applicability and cannot be extended beyond the limited range of their experimental support. Development of a general, unified theory which agrees with experiments of all kinds generally provides a far broader applicability and makes it possible to extrapolate to situations outside the range of the existing experimental support.

The present paper attempts to formulate a unified theory for the mechanical behavior of fiber-polymer laminates. A constitutive law will first be developed for laminates with unidirectional reinforcement. General laminates with multidirectional reinforcement will then be modeled as an overlay of lamina with unidirectional reinforcements of different orientations.

For fiber-polymer composites, efforts in the 1960s by Rosen [1,2], Adams and Doner [3,4], and Bažant (see Sec. 11.8 of [5]) led to highly accurate models for predicting the elastic moduli [6,7]. Many models also exist for the multiaxial strength criteria (or strength envelopes in the stress space), among which the quadratic criterion of Tsai and Wu [8] usually performs the best. The separate roles of matrix, fibers, and their interface have also been clarified.

These models, however, generally neglect the quasibrittle character of these materials. In both quasibrittle and brittle-ductile fracture, the crack tip is surrounded by a nonlinear zone that is not negligible compared to the cross-section dimension of the structures. While in brittle-ductile fracture, the fracture process zone (FPZ) at crack tip occupies a negligibly small part of the nonlinear zone, which is plastic, the FPZ in quasibrittle fracture occupies almost the entire nonlinear zone and undergoes softening damage rather than plastic deformation. The stress along the FPZ is nonuniform and the stress decreases with crack opening gradually, due to discontinuous cracking in the FPZ, crack bridging by fibers, and frictional pullout of inhomogeneities.

Aside from polymer-fiber composites, the quasibrittle materials include concrete (the archetypical case studied the earliest), rocks, stiff soils, sea ice, wood, toughened ceramics, rigid foams, paper, etc. The quasibrittle materials generally exhibit not only the statistical size effect but also a strong energetic (nonstatistical) size effect, which often dominates and is caused by stress redistribution due to formation of a large crack or large FPZ before the maximum load (for laminates, this behavior has been experimentally demonstrated for various fracture types in [9–14]. As a consequence, the fracturing behavior of quasibrittle materials and, most importantly, the energetic size effect and the quasibrittleness effect associated with structure geometry, cannot be described by means of the classical linear elastic fracture mechanics.

The energetic size effect and geometric effect of brittleness due to large tensile mode I cracks or notches, with their characteristic material length, have been described by an orthotropic generalization of Bažant's size effect law [9]. However, this model applies neither to short cracks nor initiating fractures, for which the multiaxial strength criteria are intended. For kink-band compression failure of fiber composites and the associated size effect, an adaptation of the cohesive crack model has been formulated and experimentally justified [10,15] but the model has not been extended to general multiaxial and mixed-mode loadings.

The energetic size effect at fracture initiation, which is observed in flexural failure of laminates, the size of which represents the characteristic length of the material, has recently been modeled as a consequence of stress redistribution due to formation of a boundary layer of cracking (or FPZ) and received a strong experi-

---

mental justification [11,12,16,17]. Nonetheless, the model does not apply to multiaxial loading and extends neither to post-peak crack propagation, nor to structures of negative geometry (i.e., structures in which the derivative of energy release rate with respect to crack length at constant load is negative).

The fracture energy and material characteristic length, which are most easily identified from size effect tests of notched specimens, should, in principle, allow computational predictions of damage localization and post-peak energy absorption under dynamic loadings such as impact, blast, and water or ground shock. However, such predictions are not feasible without a general model capturing also the anisotropic stiffness determined by microstructure and the multiaxial anisotropic strength criteria.

The analysis that follows is intended to make a step toward combining all the aforementioned phenomena into a single unified theory—a theory that can be used in general computer codes for predicting any behavior under general loadings. Much greater advances toward this lofty goal have already been made for other, perhaps less complicated, materials; e.g., for concrete, the microplane model, in the crack band or nonlocal setting, can approximately model the effects of random fiber reinforcement and steel reinforcing bars, the multiaxial strength criteria (with their history dependence), fracture propagation, post-peak softening, damage localization, energy absorption, and loading rate effects. For ductile metals, similar great advances have been made by Taylor models for polycrystals and Gurson's model for damage combined with plasticity theory and with material characteristic length.

It ought to be possible to achieve the same for fiber-polymer composites, despite the special complexities of their microstructure. Such an advance would allow a much more realistic analysis of large fracture-sensitive sandwich structures, such as the hulls, decks, bulkheads, masts, and antenna covers of very large and ultra-light ships made of composites, as well as load-bearing fuselage panels, wing box and rudder assemblies of large very light aircraft, or wind turbine blades, drive shafts, and containments or enclosures of various kinds. The goals and the problems are similar for carbon, glass, and aramid fibers in epoxy or vinylester matrix, and for various manufacturing techniques.

Background of Microplane Model

Inspired by the slip theory of plasticity (pioneered by Taylor [18] and formulated in detail by Batdorf and Budiansky [19]), Bažant and Oh [20,21] introduced the microplane model to simulate materials such as concrete, exhibiting softening damage. The model captures the fact that almost all of the inelastic phenomena in the concrete microstructure, including crack opening, frictional slip and dilatancy, compressive splitting with lateral spreading, and fiber break or pullout, have distinct spatial orientations that cannot be captured by the classical tensorial constitutive models exemplified by the theories of plasticity.

The microplane model rests on two basic ideas: (1) describe idealized microstructural phenomena by a constitutive relation expressed not in terms of stress and strain tensors of the macroscopic continuum, but in terms of the stress vector and strain vector acting on planes of all possible orientations at a given point of the continuum; and (2) use a variational principle to relate the microplane vectors (the micro) to the continuum tensors (the macro).

Therefore, instead of a traditional tensorial constitutive model, the microplane model uses a constitutive law formulated in terms of stress and strain vectors acting on a generic microplane. This approach has a number of advantages [22], among which the main ones are as follows. (1) Various physical phenomena are easier to formulate. (2) Various combinations of loading and unloading on different microplanes provide a rich spectrum of path dependence and automatically produce the Bauschinger effect. (3) Thanks to a vectorial constitutive description, the spatial orientations of cracking and slip can be captured (note that, for example, a relation

between the first and second invariants of the stress tensor is generally a poor characteristic of internal friction because frictional slip typically occurs on planes of one or several distinct orientations). (4) The model automatically exhibits the vertex effect, which is not captured by any of the practically usable tensorial models. (5) Interaction of microplanes provides all the cross-effects such as shear dilatancy and pressure sensitivity.

The penalty to pay for these advantages is an increased amount of computations. However, this penalty is becoming insignificant for the latest, most powerful computers. Besides, the larger the system, the smaller the penalty, because large systems are computationally dominated by the structural stiffness matrix rather than the constitutive subroutine. Systems with >10 millions of finite elements are being solved with the microplane model for concrete [23].

Since its introduction in the early 1980s, the microplane model for concrete has evolved through five progressively improved versions labeled as M1 [20,21], M2 [24], M3 [25], M4 [22,26,27], and M5 [28,29]. Microplane models have also been developed for other complex materials such as rock [30], sand, clay, rigid foam, shape memory alloys [31–33], and fiber reinforced concrete [34]. The microplane model has been generalized for finite strain in [23]. A more fundamental finite strain formulation based on thermodynamic potentials was developed in [35]. Additional microplane model formulations can also be found in [36,37].

Spectral Decomposition of the Stiffness Matrix. The elastic stress-strain relation of an anisotropic material reads, in tensorial notation,

$$\sigma_{ij} = E_{ijkl}\varepsilon_{kl} \qquad (1)$$

where the indices refer to Cartesian coordinates x_i ($i=1,2,3$); σ_{ij} and ε_{ij} are the second-order stress and strain tensors, respectively. They are symmetric and their symmetry enables their contraction into six-dimensional vectors $\boldsymbol{\sigma}$ and $\boldsymbol{\varepsilon}$. Similarly, the internal and external symmetries of the fourth-order stiffness tensor E_{ijkl} allow its contraction into a 6×6 matrix $\mathbf{E}$. The following rules contract a pair of indices into a single index: $11 \rightarrow 1$, $22 \rightarrow 2$, $33 \rightarrow 3$, $(23,32) \rightarrow 4$, $(13,31) \rightarrow 5$, and $(12,21) \rightarrow 6$. Therefore, in matrix notation we can write:

$$\boldsymbol{\sigma} = \mathbf{E}\boldsymbol{\varepsilon} \qquad (2)$$

where

$$\boldsymbol{\sigma} = [\sigma_{11}\ \sigma_{22}\ \sigma_{33}\ \sqrt{2}\sigma_{23}\ \sqrt{2}\sigma_{13}\ \sqrt{2}\sigma_{12}]^T \qquad (3)$$

$$\boldsymbol{\varepsilon} = [\varepsilon_{11}\ \varepsilon_{22}\ \varepsilon_{33}\ \sqrt{2}\varepsilon_{23}\ \sqrt{2}\varepsilon_{13}\ \sqrt{2}\varepsilon_{12}]^T \qquad (4)$$

and the matrix $\mathbf{E}$ is defined accordingly. The foregoing definitions of six-dimensional vectors are known as the *Kelvin notation* [38,39]. The factor $\sqrt{2}$ assures that both the stiffness tensor and its column matrix have the same norm, given by the sum of the squares of their elements.

By exploiting the well known spectral decomposition theorem, we can decompose the stiffness matrix [40–43] as follows:

$$\mathbf{E} = \sum_I \lambda_I \mathbf{E}_I \qquad (5)$$

where λ_I are the six eigenvalues of the stiffness matrix and $\mathbf{E}_I$ define a set of matrices constructed from the eigenvectors of $\mathbf{E}$:

$$\mathbf{E}_I = \sum_n \phi_{In}\phi_{In}^T \qquad (6)$$

where ϕ_{In} is the eigenvector associated with the eigenvalue λ_I of multiplicity n and normalized such that $\phi_{In}^T \mathbf{E}\phi_{In} = \lambda_I$. Matrices $\mathbf{E}_I$ represent a partition of unity, i.e., $\Sigma_I\mathbf{E}_I = \mathbf{1}$, they are orthogonal,
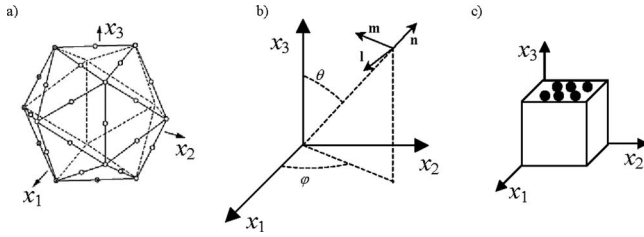
Fig. 1 (*a*) Microplane orientations (normals defined by radial lines through circled points); (*b*) spherical coordinate system; and (*c*) coordinate system for laminates

i.e., $\mathbf{E}_I\mathbf{E}_J=\mathbf{0}$ if $I\neq J$, and idempotent, i.e., $\mathbf{E}_I\mathbf{E}_I=\mathbf{E}_I$.

The same matrices $\mathbf{E}_I$ also decompose the stress and strain vectors into energetically orthogonal modes, which are called eigenstresses and eigenstrains and are defined as:

$$\boldsymbol{\sigma}_I = \mathbf{E}_I\boldsymbol{\sigma} \tag{7}$$

$$\boldsymbol{\varepsilon}_I = \mathbf{E}_I\boldsymbol{\varepsilon} \tag{8}$$

It is easy to show that $\boldsymbol{\sigma}=\Sigma_I\boldsymbol{\sigma}_I$, $\boldsymbol{\varepsilon}=\Sigma_I\boldsymbol{\varepsilon}_I$, and $\boldsymbol{\sigma}_I=\lambda_I\boldsymbol{\varepsilon}_I$. In the case of isotropic materials, the decomposition of stresses and strains in Eqs. (7) and (8) represents the well known volumetric-deviatoric decomposition.

The spectral decomposition theorem can be applied to the compliance matrix $\mathbf{C}=\mathbf{E}^{-1}$ with a similar result:

$$\mathbf{C} = \sum_I \lambda_I^{-1}\mathbf{E}_I \tag{9}$$

Note that in this case the eigenvalues are the inverse of the eigenvalues of the corresponding stiffness matrix, while the matrices $\mathbf{E}_I$ are the same.

Microplane Model Formulation With Spectral Decomposition. At the microstructural level of a material, nonlinear and inelastic phenomena often occur on planes of a certain specific orientation. Therefore, the constitutive law characterizing the mechanical behavior is best described through a relation between stress and strain vectors acting on a generic plane of arbitrary spatial orientation. These planes, called the microplanes [20,21], can be imagined as the tangent planes of a unit sphere surrounding every point in the three-dimensional space (Fig. 1(*a*)).

There are two different classes of microplane models: the kinematically constrained and the statically constrained. In the kinematically constrained microplane model (introduced by Bažant and Oh in [20,21]), the strain vector on each microplane is the projection of the macroscopic strain tensor. By using the Kelvin notation, we can write:

$$\boldsymbol{\varepsilon}_{\mathcal{P}} = \mathcal{P}\boldsymbol{\varepsilon} \tag{10}$$

where $\boldsymbol{\varepsilon}_{\mathcal{P}}=[\varepsilon_N\ \varepsilon_M\ \varepsilon_L]^T$ is the microplane strain vector, with ε_N=normal strain component, ε_M and ε_L=shear strain components, and

$$\mathcal{P} = \begin{bmatrix} N_{11} & N_{22} & N_{33} & \sqrt{2}N_{23} & \sqrt{2}N_{13} & \sqrt{2}N_{12} \\ M_{11} & M_{22} & M_{33} & \sqrt{2}M_{23} & \sqrt{2}M_{13} & \sqrt{2}M_{12} \\ L_{11} & L_{22} & L_{33} & \sqrt{2}L_{23} & \sqrt{2}L_{13} & \sqrt{2}L_{12} \end{bmatrix} \tag{11}$$

Matrix $\mathcal{P}$ collects the components of the tensors $N_{ij}=n_in_j$, $M_{ij}=(m_in_j+m_jn_i)/2$, and $L_{ij}=(l_in_j+l_jn_i)/2$, where n_i, m_i, and l_i are local Cartesian coordinate vectors on the generic microplane, with n_i being normal. If the microplane orientation is defined by spherical angles ϑ and φ (Fig. 1(*b*)), then $n_1=\sin\vartheta\cos\varphi$, $n_2=\sin\vartheta\sin\varphi$, $n_3=\cos\vartheta$, and one can choose $m_1=\cos\vartheta\cos\varphi$, $m_2=\cos\vartheta\sin\varphi$, $m_3=-\sin\vartheta$, which gives $l_1=-\sin\varphi$, $l_2=\cos\varphi$,

and $l_3=0$.

By the spectral decomposition of the strain tensor and a separate projection of each eigenstrain, we can also decompose the microplane strain vector into microplane eigenstrains as:

$$\boldsymbol{\varepsilon}_{\mathcal{P}} = \sum_I \boldsymbol{\varepsilon}_{\mathcal{P}I} \tag{12}$$

where $\boldsymbol{\varepsilon}_{\mathcal{P}I}=\mathcal{P}\boldsymbol{\varepsilon}_I=\mathcal{P}_I\boldsymbol{\varepsilon}$, with $\mathcal{P}_I=\mathcal{P}\mathbf{E}_I$. The split of the microplane strain vector introduced in Eq. (12) is an anisotropic generalization of the volumetric-deviatoric split introduced in the isotropic microplane model in [24,22].

From the microplane eigenstrains, the microplane eigenstresses $\boldsymbol{\sigma}_{\mathcal{P}I}$ are calculated according to the constitutive relations for the normal and shear components of each eigenmode: $\sigma_{NI}=\mathcal{F}_{NI}(\boldsymbol{\varepsilon}_{\mathcal{P}1},\boldsymbol{\varepsilon}_{\mathcal{P}2},\ldots)$, $\sigma_{MI}=\mathcal{F}_{MI}(\boldsymbol{\varepsilon}_{\mathcal{P}1},\boldsymbol{\varepsilon}_{\mathcal{P}2},\ldots)$, and $\sigma_{LI}=\mathcal{F}_{LI}(\boldsymbol{\varepsilon}_{\mathcal{P}1},\boldsymbol{\varepsilon}_{\mathcal{P}2},\ldots)$.

The macroscopic stress tensor may then be computed from the principle of virtual work, which reads:

$$\boldsymbol{\sigma} = \frac{3}{2\pi}\sum_I \int_\Omega \mathcal{P}_I^T\boldsymbol{\sigma}_{\mathcal{P}I}\mathrm{d}\Omega \tag{13}$$

where Ω is the surface of a unit hemisphere. This principle represents a weak variational constraint. In general, the projection of the stress tensor does not coincide with the microplane eigenstress: $\boldsymbol{\sigma}_{\mathcal{P}I}\neq\mathcal{P}_I\boldsymbol{\sigma}$. Nevertheless, such a coincidence, called the double constraint, holds in the elastic regime if and only if the microplane eigenstress vector is proportional to the microplane eigenstrain vector through the associated eigenvalue:

$$\boldsymbol{\sigma}_{\mathcal{P}I} = \lambda_I\boldsymbol{\varepsilon}_{\mathcal{P}I} \tag{14}$$

In this particular case, recalling that $\boldsymbol{\varepsilon}_{\mathcal{P}I}=\mathcal{P}_I\boldsymbol{\varepsilon}$ with $\mathcal{P}_I=\mathcal{P}\mathbf{E}_I$, from Eq. (13) we obtain:

$$\boldsymbol{\sigma}_{\mathcal{P}I} = \mathcal{P}_I\boldsymbol{\sigma} = \mathcal{P}\mathbf{E}_I\left[\frac{3}{2\pi}\sum_I \int_\Omega \mathbf{E}_I\mathcal{P}^T\lambda_I\mathcal{P}\mathbf{E}_I\boldsymbol{\varepsilon}\mathrm{d}\Omega\right]$$

$$= \mathcal{P}\mathbf{E}_I\sum_I \lambda_I\mathbf{E}_I\frac{3}{2\pi}\int_\Omega \mathcal{P}^T\mathcal{P}\mathrm{d}\Omega\mathbf{E}_I\boldsymbol{\varepsilon} \tag{15}$$

Moreover, it can be proven that:

$$\frac{3}{2\pi}\int_\Omega \mathcal{P}^T\mathcal{P}\mathrm{d}\Omega = \mathbf{1} \tag{16}$$

Therefore, from Eq. (15) we obtain:

$$\mathcal{P}_I\boldsymbol{\sigma} = \mathcal{P}\mathbf{E}_I\sum_J \lambda_J\mathbf{E}_J\mathbf{E}_J\boldsymbol{\varepsilon} = \mathcal{P}\lambda_I\mathbf{E}_I\mathbf{E}_I\mathbf{E}_I\boldsymbol{\varepsilon} = \lambda_I\mathcal{P}\mathbf{E}_I\boldsymbol{\varepsilon} = \lambda_I\mathcal{P}_I\boldsymbol{\varepsilon}$$

$$= \lambda_I\boldsymbol{\varepsilon}_{\mathcal{P}I} \tag{17}$$

which proves the existence of a double constraint for elastic behavior.

In a statically constrained microplane model, the microplane stress vectors are the projections of the macroscopic stress tensor

$$\boldsymbol{\sigma}_{\mathcal{P}} = \mathcal{P}\boldsymbol{\sigma} \tag{18}$$

or, equivalently, by introducing the spectral decomposition of stresses:

$$\boldsymbol{\sigma}_{\mathcal{P}} = \sum_I \boldsymbol{\sigma}_{\mathcal{P}I}, \quad \boldsymbol{\sigma}_{\mathcal{P}I} = \mathcal{P}\boldsymbol{\sigma}_I = \mathcal{P}_I\boldsymbol{\sigma} \tag{19}$$

After formulating suitable constitutive relations at the microplane level, it is possible to obtain the microplane strains from the microplane stresses as: $\varepsilon_{NI}=\mathcal{G}_{NI}(\boldsymbol{\sigma}_{\mathcal{P}1},\boldsymbol{\sigma}_{\mathcal{P}2},\ldots)$, $\varepsilon_{MI}=\mathcal{G}_{MI}(\boldsymbol{\sigma}_{\mathcal{P}1},\boldsymbol{\sigma}_{\mathcal{P}2},\ldots)$, and $\varepsilon_{LI}=\mathcal{G}_{LI}(\boldsymbol{\sigma}_{\mathcal{P}1},\boldsymbol{\sigma}_{\mathcal{P}2},\ldots)$. The macroscopic strain is then obtained by imposing the principle of complementary virtual work, which reads:

$$\boldsymbol{\varepsilon} = \frac{3}{2\pi}\sum_I \int_\Omega \boldsymbol{\mathcal{P}}_I^T \boldsymbol{\varepsilon}_{\mathcal{P}I}\mathrm{d}\Omega \qquad (20)$$

In this case the microplane strains are generally not the projections of the macroscopic strains: $\boldsymbol{\varepsilon}_{\mathcal{P}I} \neq \boldsymbol{\mathcal{P}}_I\boldsymbol{\varepsilon}$. Nevertheless, as seen earlier for the kinematically constrained microplane model, the double constraint holds in the elastic regime ($\boldsymbol{\varepsilon}_{\mathcal{P}I} = \lambda_I^{-1}\boldsymbol{\sigma}_{\mathcal{P}I}$).

Comparison With Alternative Formulations

Brocca et al. [33] proposed an alternative microplane formulation for anisotropic materials based on the assumption that the elastic moduli on the microplanes vary ellipsoidally as a function of the microplane orientation:

$$E_i(\varphi,\theta) = E_{i1}\sin\theta\cos\varphi + E_{i2}\sin\theta\sin\varphi + E_{i3}\cos\theta \quad (21)$$

where φ and θ are the angles characterizing the normal direction of a generic microplane in spherical coordinates (Fig. 1(b)). Subscript $i = N, M, L$ labels the components of the microplane strain and stress vectors, and E_{i1}, E_{i2}, E_{i3} are the microplane elastic moduli in the x_1-, x_2-, and x_3-directions, respectively. This approach can be used to approximatively represent the behavior of a mildly anisotropic material such as a PVC foam. However, it cannot represent correctly the mechanical properties of strongly anisotropic materials such as fiber composite laminates. This can be easily proven by computing the elastic stiffness matrix arising from Eq. (21).

By integrating the microplane elastic energy over the unit hemisphere, we obtain:

$$\mathcal{W} = \frac{3}{2\pi}\int_\Omega \frac{1}{2}\boldsymbol{\sigma}_\mathcal{P}^T \mathbf{E}_\mathcal{P}\boldsymbol{\sigma}_\mathcal{P}\mathrm{d}\Omega = \frac{1}{2}\boldsymbol{\sigma}^T\left[\frac{3}{2\pi}\int_\Omega \boldsymbol{\mathcal{P}}^T\mathbf{E}_\mathcal{P}\boldsymbol{\mathcal{P}}\mathrm{d}\Omega\right]\boldsymbol{\sigma}$$

$$(22)$$

where matrix $\mathbf{E}_\mathcal{P} = \mathrm{diag}(E_i)$. The equivalent stiffness matrix is defined as:

$$\mathbf{E}^* = \frac{3}{2\pi}\int_\Omega \boldsymbol{\mathcal{P}}^T\mathbf{E}_\mathcal{P}\boldsymbol{\mathcal{P}}\mathrm{d}\Omega \qquad (23)$$

The stiffness matrix $\mathbf{E}$ of a generic orthotropic material depends on nine independent constants that must be uniquely related to the nine parameters in Eq. (21) if the exact correspondence between this microplane formulation and the tensorial formulation holds. To determine that relationship, we can try to solve the system of simultaneous equations obtained by equating each element of matrix $\mathbf{E}$ to the corresponding element of matrix $\mathbf{E}^*$ (note that the elements of $\mathbf{E}^*$ are a linear combination of the microplane elastic moduli E_{i1}, E_{i2}, and E_{i3}). Such a system of equations reads

$$\mathbf{Y} = \mathbf{AX} \qquad (24)$$

where

$$\mathbf{Y} = [E_{11}, E_{22}, E_{33}, E_{12}, E_{13}, E_{23}, E_{44}, E_{55}, E_{66}]^T \qquad (25)$$

$$\mathbf{X} = [E_{N1}, E_{N2}, E_{N3}, E_{M1}, E_{M2}, E_{M3}, E_{L1}, E_{L2}, E_{L3}]^T \qquad (26)$$

It can be shown that the rank of matrix $\mathbf{A}$ is 6, whereas 9 would be required to solve the system (24). Therefore, if an ellipsoidal formulation for the microplane moduli is used as indicated in Eq. (21), it is impossible to represent the material behavior in the elastic range since an exact correspondence with the tensorial model cannot be obtained. In particular, the lower rank of the matrix demonstrates that the ellipsoidal formulation implies a higher number of symmetries than those implied by material orthotropy. Only the microplane formulation based on spectral decomposition of the stiffness tensor guarantees that an exact correspondence in elasticity between tensorial macrostiffness and vectorial microstiffness can be established.

A similar limitation can be shown for the microplane models developed for mildly anisotropic clay in [31,44].

Transverse Isotropy: Analysis of Microplane Eigenmodes

Let us now consider the case of transverse isotropy, which is relevant to unidirectional laminates. We introduce a cartesian coordinate system whose axis x_3 coincides with the direction of the fibers (Fig. 1(c)). This axis is orthogonal to the plane of isotropy of the material. Let the *longitudinal* direction be the direction of the fibers (axis x_3), and let the *transverse* directions be all those orthogonal to the fibers. The elastic compliance matrix for a transversely isotropic material is given by:

$$\mathbf{C} = \begin{bmatrix} 1/E_T & -\nu_T/E_T & -\nu_L/E_T & 0 & 0 & 0 \\ -\nu_T/E_T & 1/E_T & -\nu_L/E_T & 0 & 0 & 0 \\ -\nu_L/E_T & -\nu_L/E_T & 1/E_L & 0 & 0 & 0 \\ 0 & 0 & 0 & 1/(2G_L) & 0 & 0 \\ 0 & 0 & 0 & 0 & 1/(2G_L) & 0 \\ 0 & 0 & 0 & 0 & 0 & (1+\nu_T)/E_T \end{bmatrix} \qquad (27)$$

where E_L, E_T = Young's moduli in the longitudinal and transverse directions, respectively, G_L = out-of-plane shear modulus, ν_L, ν_T = Poisson ratios in the longitudinal and transverse directions, respectively.

Following [43], the eigenvalues of the compliance matrix, which are the reciprocal of the eigenvalues λ_I of the stiffness matrix, can be expressed as:

$$\lambda_1^{-1} = \frac{1+\nu_T}{E_T} = \frac{1}{2G_T} \qquad (28)$$

$$\lambda_2^{-1} = \frac{1-\nu_T}{2E_T} + \frac{1}{2E_L} - \left[\left(\frac{1-\nu_T}{2E_T} - \frac{1}{2E_L}\right)^2 + \frac{2\nu_L^2}{E_T^2}\right]^{1/2} \qquad (29)$$

$$\lambda_3^{-1} = \frac{1-\nu_T}{2E_T} + \frac{1}{2E_L} + \left[\left(\frac{1-\nu_T}{2E_T} - \frac{1}{2E_L}\right)^2 + \frac{2\nu_L^2}{E_T^2}\right]^{1/2} \qquad (30)$$

$$\lambda_4^{-1} = \frac{1}{2G_L} \qquad (31)$$

and the idempotent matrices decomposing $\mathbf{E}$ are

Table 1 Microplane strain modes: Normal component

Mode	ε_N
I	$\sin^2\theta[\alpha_1(\cos^2\varphi-\sin^2\varphi)+2\sqrt{2}\varepsilon_6\sin\varphi\cos\varphi]$
II	$\alpha_2(-\sin\omega\sin^2\theta/\sqrt{2}+\cos\omega\cos^2\theta)$
III	$\alpha_3(\cos\omega\sin^2\theta/\sqrt{2}+\sin\omega\cos^2\theta)$
IV	$2\sqrt{2}\sin\theta\cos\theta(\varepsilon_4\sin\varphi+\varepsilon_5\cos\varphi)$

$$\mathbf{E}_1 = \begin{bmatrix} 1/2 & -1/2 & 0 & 0 & 0 & 0 \\ -1/2 & 1/2 & 0 & 0 & 0 & 0 \\ 0 & 0 & 0 & 0 & 0 & 0 \\ 0 & 0 & 0 & 0 & 0 & 0 \\ 0 & 0 & 0 & 0 & 0 & 0 \\ 0 & 0 & 0 & 0 & 0 & 1 \end{bmatrix} \qquad (32)$$

$$\mathbf{E}_2 = \begin{bmatrix} c^2/2 & c^2/2 & cs/\sqrt{2} & 0 & 0 & 0 \\ c^2/2 & c^2/2 & cs/\sqrt{2} & 0 & 0 & 0 \\ cs/\sqrt{2} & cs/\sqrt{2} & s^2 & 0 & 0 & 0 \\ 0 & 0 & 0 & 0 & 0 & 0 \\ 0 & 0 & 0 & 0 & 0 & 0 \\ 0 & 0 & 0 & 0 & 0 & 0 \end{bmatrix} \qquad (33)$$

$$\mathbf{E}_3 = \begin{bmatrix} s^2/2 & s^2/2 & -cs/\sqrt{2} & 0 & 0 & 0 \\ s^2/2 & s^2/2 & -cs/\sqrt{2} & 0 & 0 & 0 \\ -cs/\sqrt{2} & -cs/\sqrt{2} & c^2 & 0 & 0 & 0 \\ 0 & 0 & 0 & 0 & 0 & 0 \\ 0 & 0 & 0 & 0 & 0 & 0 \\ 0 & 0 & 0 & 0 & 0 & 0 \end{bmatrix} \qquad (34)$$

$$\mathbf{E}_4 = \begin{bmatrix} 0 & 0 & 0 & 0 & 0 & 0 \\ 0 & 0 & 0 & 0 & 0 & 0 \\ 0 & 0 & 0 & 0 & 0 & 0 \\ 0 & 0 & 0 & 1 & 0 & 0 \\ 0 & 0 & 0 & 0 & 1 & 0 \\ 0 & 0 & 0 & 0 & 0 & 0 \end{bmatrix} \qquad (35)$$

where $c=\cos\omega$, $s=\sin\omega$, and ω is the so-called eigenangle defined as:

$$\tan 2\omega = \frac{-2\sqrt{2}\nu_L/E_T}{(1-\nu_T)/E_T-1/E_L} \qquad (36)$$

The projection of the strain modes defined in Eq. (8) on a generic microplane gives the microplane strain distribution in Tables 1 and 2, where $\alpha_1=(\varepsilon_1-\varepsilon_2)/2$, $\alpha_2=-\sin\omega(\varepsilon_1+\varepsilon_2)/\sqrt{2}+\varepsilon_3\cos\omega$, and $\alpha_3=\cos\omega(\varepsilon_1+\varepsilon_2)/\sqrt{2}+\varepsilon_3\sin\omega$.

Let us now consider the distribution of the normal strain components on the microplane sphere caused by a uniaxial strain applied at the macroscale in the longitudinal direction (i.e., along the
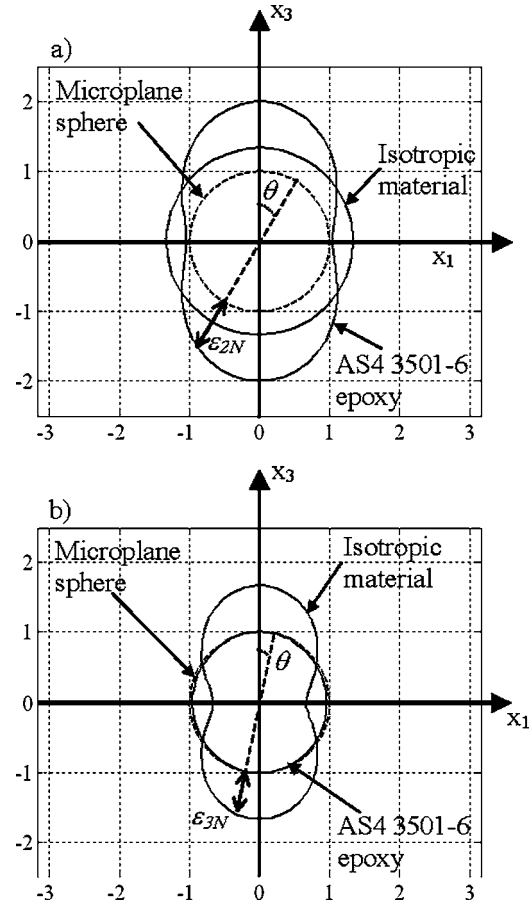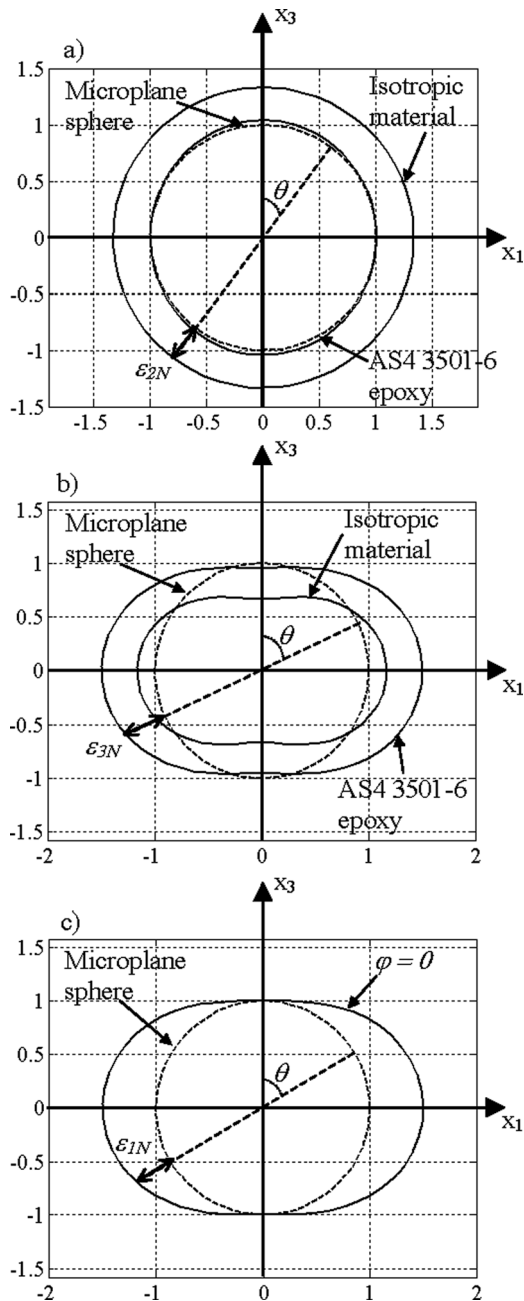
Fig. 2 Effect of a macroscopic strain applied in fiber direction on (a) mode II, and (b) mode III

x_3-axis). Strain mode I and strain mode IV are exactly zero because they do not depend on ε_3. Strain mode II and strain mode III are nonzero and they depend on the eigenangle ω. Figures 2(a) and 2(b) show the microplane normal strain distribution of modes II and III for isotropic materials ($\omega=0.615$) and for a highly anisotropic carbon-epoxy composite (AS4 3501-6/epoxy with $\omega=0.06$). For isotropic materials, mode II coincides with the volumetric strain mode, and mode III with the deviatoric strain mode. On the contrary, for the composite considered, mode II mostly loads the microplanes whose normal orientation is close to the direction of the fibers, and mode III almost vanishes.

A different picture arises if we consider a uniaxial strain at the macroscale applied in the transverse direction (x_1-axis). In this case the only mode that is exactly zero is mode IV. Figures 3(a)–3(c) show the microplane normal strain distribution of modes II, III, and I, respectively. For the isotropic case, strain mode II coincides again with the volumetric strain mode, and the sum of mode I and mode III coincides with the deviatoric strain mode. Mode II vanishes and modes I and II mostly load the microplanes whose orientation is close to the direction orthogonal to

Table 2 Microplane strain modes: Tangential components

Mode	ε_M	ε_L
I	$\sin\theta\cos\theta[\alpha_1(\cos^2\varphi-\sin^2\varphi)+2\sqrt{2}\varepsilon_4\sin\varphi\cos\varphi]$	$\sin\theta[\alpha_1\sin\varphi\cos\varphi+\sqrt{2}\varepsilon_6(\cos^2\varphi-\sin^2\varphi)]$
II	$\alpha_2\sin\theta\cos\theta(-\sin\omega/\sqrt{2}-\cos\omega)$	0
III	$\alpha_3\sin\theta\cos\theta(\cos\omega/\sqrt{2}-\sin\omega)$	0
IV	$\sqrt{2}(\cos^2\theta-\sin^2\theta)(\varepsilon_4\sin\varphi+\varepsilon_5\cos\varphi)$	$\sqrt{2}\cos\theta(\varepsilon_4\cos\varphi-\varepsilon_5\sin\varphi)$

Fig. 3 Effect of a macroscopic strain applied in transverse direction on (*a*) mode II, (*b*) mode III, and (*c*) mode I

the fibers. Note that strain mode I consists of a deviatoriclike mode in the plane of isotropy of the unidirectional laminate (see Table 1).

This analysis shows that the response of the composite material subjected to strain mode II strongly depends on the behavior of the fibers whereas material response under modes I and III is dominated by the behavior of the matrix.

Strain mode IV is a pure-shear strain mode loading the microplanes in such a way that generally both the matrix and the fibers have an effect. Nevertheless, in the following formulation, we will assume the shear resistance of the fibers to vanish.

Nonlinear and Softening Behavior of Unidirectional Laminates. The macroscopic behavior of composite laminates, in both linear and nonlinear range, is governed by various phenomena occurring in a material microstructure with the three phases—

the fibers, matrix, and fiber-matrix interface. The mechanics of these phenomena, which include microcracking, stress redistribution among the phases, fiber pull-out, fiber-matrix debonding, fiber buckling, etc., should be included in formulating constitutive laws that aim at real predictive capability. However, in practice, the complexity and the lack of accurate knowledge of the details of microstructural behavior impede attaining this aim and the only option available is a phenomenological approach. That is particularly true for tensorial constitutive laws.

The microplane framework, in which the constitutive laws are formulated in terms of vectors acting on planes of many specified orientations, provides more flexibility than the classical tensorial framework and allows introducing in the formulation some microstructural features even in a phenomenological setting. In what follows, the constitutive law at the microplane level is formulated and physically justified on the basis of current knowledge of damage and failure of the composite laminate microstructure.

Exploiting the experience with microplane models for concrete, rocks, and soils developed by Bažant and co-workers since the early eighties, we introduce for the stress-strain constitutive relation at the microplane level a kinematic constraint of the microplanes, and we adopt the concept of stress-strain boundary (or strain-dependent yield limit) introduced in [25] and used in microplane models M4, M5, and M5f [22,27,28,34]. According to that concept, for each strain mode, each stress component at the microplane level must satisfy the following inequalities

$$\mathcal{F}_{NI}^- \le \sigma_{NI} \le \mathcal{F}_{NI}^+, \quad |\sigma_{MI}| \le \mathcal{F}_{TI}, \quad |\sigma_{LI}| \le \mathcal{F}_{TI} \qquad (37)$$

where $\mathcal{F}_{NI}^-$=compression boundary, $\mathcal{F}_{NI}^+$=tension boundary, and $\mathcal{F}_{TI}$=shear boundary.

Note that, from the viewpoint of invariance with respect to rotations of microplane coordinates about the normal to the microplane, the shear boundary would be expressed more accurately in terms of the total shear stress $\sigma_{TI}=(\sigma_{MI}^2+\sigma_{LI}^2)^{1/2}$ instead of the separate components σ_{MI} and σ_{LI}. However, the boundaries in Eq. (37), expressed in terms of components σ_{MI} and σ_{LI}, lead to simpler and more stable numerical implementation and give about the same results on the macrolevel.

The boundaries for the normal component of each mode (I =I, ... ,IV) can be formulated as follows:

$$\mathcal{F}_{NI}^+ = t_I(\theta)\prod_{J=1}^{4} f_{IJ}^+(\boldsymbol{\varepsilon}_{\mathcal{P}J}, \theta), \quad \mathcal{F}_{NI}^- = -c_I(\theta)\prod_{J=1}^{4} f_{IJ}^-(\boldsymbol{\varepsilon}_{\mathcal{P}J}, \theta) \quad (38)$$

in which angle θ gives the position of a generic point along the meridians of the unit hemisphere (Fig. 1(*b*)). For $\theta=0$, Eqs. (38) characterize the nonlinear behavior in the direction of the fibers, and for $\theta=\pi/2$, in the direction of the matrix. Because of the transverse isotropy, Eqs. (38) do not involve the angle φ giving the position along the parallels of the unit hemisphere (Fig. 1(*b*)).

The products in Eqs. (38) describe the interaction between different strain modes. In particular, each function $f_{IJ}(\boldsymbol{\varepsilon}_{\mathcal{P}J})$ gives the effect of strain mode J on the response of mode I. Obviously, if $f_{IJ}(\boldsymbol{\varepsilon}_{\mathcal{P}J}) \equiv 1$ for $I \ne J$, then the strain modes are completely uncoupled. Furthermore, if $f_{II}(\boldsymbol{\varepsilon}_{\mathcal{P}J}) \equiv 1$ also, the behavior is purely plastic. For the plastic case, the distribution of the microplane yield strengths in tension and compression is given by $t_I(\theta)$ and $c_I(\theta)$, respectively. Note that, in the general case, $t_I(\theta)$ and $c_I(\theta)$ do not necessarily represent the microplane strength and must be regarded only as reference strengths.

Similarly, the boundary for the shear components can be formulated as:

$$\mathcal{F}_{TI} = s_I(\theta) \prod_{J=1}^{4} g_{IJ}(\boldsymbol{\varepsilon}_{\mathcal{P}J}, \theta) \qquad (39)$$

where $s_I(\theta)$ are the shear reference strengths for each mode and functions $g_{IJ}(\boldsymbol{\varepsilon}_{\mathcal{P}J}, \theta)$ have the same meaning as functions $f_{IJ}(\boldsymbol{\varepsilon}_{\mathcal{P}J}, \theta)$ featured by the normal boundaries.

Longitudinal Tension and Compression. Except for a minor effect of fiber undulations, the matrix and fibers work in parallel coupling when the composite is subjected to tension or compression in the direction of the fibers.

In tension, the nonlinear behavior starts when the elastic limit is reached in the matrix whose strength is significantly lower than the strength of the fibers. At this point, the fibers are still in the elastic phase and, consequently, stresses can be redistributed in the microstructure, allowing an overall increase of the applied load. The maximum carrying capacity of the unidirectional laminate is attained when the second phase (fibers) fails. However, the fibers do not fail simultaneously and then it is reasonable to assume a gradual reduction of the macroscopic stress (or softening) with increasing macroscopic strain. The existence of softening quasibrittle behavior has been experimentally confirmed by recent size effect studies [11].

In the case of compression, the failure is dominated by various instability modes at the microscopic level [2]. For a low volume fraction of fibers, compression usually causes fiber kinking due to microbuckling. For a relatively high volume fraction of fibers, microbuckling is typically associated with the formation of a kink band that propagates transversely to the fibers. Very high values of fiber volume fraction usually prevent microbuckling and the laminate suffers shear failure. Again, as for the case of tension during failure, a certain degree of stress redistribution occurs in the microstructure, and then the loss of carrying capacity is gradual as the strain increases.

As shown in the preceding sections, mode II is the strain mode that is activated mainly by loading the material in the longitudinal direction (i.e., the direction of fibers). Thus, the behavior highlighted above can be analytically approximated through the definition of boundaries on mode II normal and shear components. This is achieved by setting:

$$t_2(\theta) = t_{20} \cos^2 \theta, \quad c_2(\theta) = c_{20} \cos^2 \theta, \quad s_2(\theta) = s_{20} \qquad (40)$$

$$f_{22}^+(\boldsymbol{\varepsilon}_{\mathcal{P}2}) = 1 - \frac{\varepsilon_2^+ - k_{2i}^+}{k_{2f}^+}, \quad f_{22}^-(\boldsymbol{\varepsilon}_{\mathcal{P}2}) = 1 - \frac{|\varepsilon_2^-| - k_{2i}^-}{k_{2f}^-}$$

$$g_{22}(\boldsymbol{\varepsilon}_{\mathcal{P}2}) = f_{22}^+(\boldsymbol{\varepsilon}_{\mathcal{P}2}) f_{22}^-(\boldsymbol{\varepsilon}_{\mathcal{P}2}) \qquad (41)$$

with the conditions $1 \le f_{22}^+(\boldsymbol{\varepsilon}_{\mathcal{P}2}) \le 0$ and $1 \le f_{22}^-(\boldsymbol{\varepsilon}_{\mathcal{P}2}) \le 0$.

The preceding equations represent linear softening laws for the normal component in tension and compression while the softening evolution of the shear component is assumed to be proportional to the normal boundaries. t_{20}, c_{20}, and s_{20} are mode II strengths in tension, compression and shear, respectively. ε_2^+ and ε_2^- are the equivalent strains in tension and compression, respectively, which couple the effect of shear and normal microplane strains. They are defined as $\varepsilon_2^+ = \max(\varepsilon_2)$ and $\varepsilon_2^- = \min(\varepsilon_2)$, where $\varepsilon_2 = \text{sign}(\varepsilon_{N2}) \times [\varepsilon_{N2}^2 + \varepsilon_{M2}^2 + \varepsilon_{L2}^2]^{1/2} \times k_{2i}^+$ and k_{2f}^+ are two material parameters: k_{2i}^+ defines the tensile strain at which the behavior becomes softening, and $k_{2i}^+ + k_{2f}^+$ is the tensile strain at which the carrying capacity is completely exhausted. k_{2i}^- and k_{2f}^- have the same meaning as k_{2i}^+ and k_{2f}^+ but for compression.

Transverse Tension and Compression. Tensile behavior in the direction perpendicular to the fibers is mainly controlled by the fiber-matrix interface. Failure is usually caused by stress concentration at the interface followed by the propagation of cracks around the fibers [3]. Failure in compression in the transverse direction is induced by stress concentration in the microstructure,

which leads to the failure of one of the three phases of the composite. In particular, one of the following failure modes may occur: (1) crushing of the matrix, (2) crushing of the fibers, and (3) fiber-matrix debonding followed by a macroscopic shear failure.

The modes relevant to these phenomena are strain modes I and III because they mainly load microplanes in the transverse direction (Table 1). Since the failure modes described above are related mainly to the composite matrix, we can reasonably assume that the associated reference strengths, in both tension, compression, and shear, do not depend on the orientation (angle θ): $t_1(\theta) = t_{10}$, $t_3(\theta) = t_{30}$, $c_1(\theta) = c_{10}$, $c_3(\theta) = c_{30}$, $s_1(\theta) = s_{10}$, and $s_3(\theta) = s_{30}$.

As for the case of the strain mode II, the post-peak behavior of mode I and mode III is formulated through linear softening constitutive laws. Since strain mode I is quasideviatoric in the plane of symmetry of the unidirectional laminate, both compression and tension appear at the microplane level regardless of the sign of the macroscopic strains in the transverse direction. This does not help to simulate the lack of symmetry between matrix failures in tension and compression. The only way to distinguish between these two types of failure is to let the behavior of strain mode I be dependent on the mean stress in the plane of isotropy: $\bar{\sigma} = (\sigma_{11} + \sigma_{22})/2$. The mode I boundaries are formulated as follows:

$$f_{11}^+(\boldsymbol{\varepsilon}_{\mathcal{P}1}) = 1 - \frac{\varepsilon_1^+ - k_{1i\alpha}^+}{k_{1f\alpha}^+}, \quad f_{11}^-(\boldsymbol{\varepsilon}_{\mathcal{P}1}) = 1 - \frac{|\varepsilon_1^-| - k_{1i\alpha}^-}{k_{1f\alpha}^-}, \quad (\bar{\sigma} \ge 0)$$

$$(42)$$

and

$$f_{11}^+(\boldsymbol{\varepsilon}_{\mathcal{P}1}) = 1 - \frac{\varepsilon_1^+ - k_{1i\beta}^+}{k_{1f\beta}^+}, \quad f_{11}^-(\boldsymbol{\varepsilon}_{\mathcal{P}1}) = 1 - \frac{|\varepsilon_1^-| - k_{1i\beta}^-}{k_{1f\beta}^-}, \quad (\bar{\sigma} < 0)$$

$$(43)$$

always subjected to the conditions $1 \le f_{11}^+(\boldsymbol{\varepsilon}_{\mathcal{P}1}) \le 0$ and $1 \le f_{11}^-(\boldsymbol{\varepsilon}_{\mathcal{P}1}) \le 0$; ε_1^+ and ε_1^- are equivalent strains in tension and compression, respectively, as defined in the case of mode II, and $k_{1i\alpha}^+, \dots, k_{1f\beta}^+$ are material parameters.

The boundaries for mode III are formulated as follows:

$$f_{33}^+(\boldsymbol{\varepsilon}_{\mathcal{P}1}) = h_3 - \frac{\varepsilon_3^+ - h_3 k_{3i}^+}{k_{3f}^+}, \quad f_{33}^-(\boldsymbol{\varepsilon}_{\mathcal{P}3}) = 1 - \frac{|\varepsilon_3^-| - k_{3i}^-}{k_{3f}^-} \qquad (44)$$

with the conditions $h_3 \le f_{33}^+(\boldsymbol{\varepsilon}_{\mathcal{P}3}) \le 0$ and $1 \le f_{33}^-(\boldsymbol{\varepsilon}_{\mathcal{P}3}) \le 0$. Again, ε_3^+ and ε_3^- are equivalent strains, and $k_{3i}^+, \dots, k_{3f}^-$ are material parameters; h_3 is a function of the normal strain of mode II and it is introduced in the formulation of mode III in tension in order to prevent an unrealistic splitting-like failure associated with longitudinal compression: $h_3 = 1$ for $\varepsilon_{N2} > 0$ and $h_3 = 1 + h_{30} \varepsilon_2$ for $\varepsilon_{N2} < 0$.

For both mode I and mode III, the shear boundary is formulated through the product of tensile and compressive normal boundaries: $g_{11}(\boldsymbol{\varepsilon}_{\mathcal{P}1}) = f_{11}^+(\boldsymbol{\varepsilon}_{\mathcal{P}1}) f_{11}^-(\boldsymbol{\varepsilon}_{\mathcal{P}1})$ and $g_{33}(\boldsymbol{\varepsilon}_{\mathcal{P}3}) = f_{33}^+(\boldsymbol{\varepsilon}_{\mathcal{P}3}) f_{33}^-(\boldsymbol{\varepsilon}_{\mathcal{P}3})$.

In-Plane Shear. When the composite is subjected to in-plane shear, high stress concentrations at the matrix-fiber interface usually lead to shear failure in the matrix or to fiber-matrix debonding, or to both [4]. The fibers have, in this situation, little effect and so the relevant microplane boundary (mode IV) can be assumed not to depend on the orientation. Consequently, the tensile and compressive microplane strengths read $t_4(\theta) = t_{40}$, $c_4(\theta) = c_{40}$, $s_4(\theta) = s_{40}$. Similar to the other cases, the softening evolution can be expressed as

$$f_{44}^+(\boldsymbol{\varepsilon}_{\mathcal{P}4}) = 1 - \frac{\varepsilon_4^+ - k_{4i}^+}{k_{4f}^+}, \quad f_{44}^-(\boldsymbol{\varepsilon}_{\mathcal{P}4}) = 1 - \frac{|\varepsilon_4^-| - k_{4i}^-}{k_{4f}^-}$$

$$g_{44}(\boldsymbol{\varepsilon}_{\mathcal{P}4}) = f_{44}^+(\boldsymbol{\varepsilon}_{\mathcal{P}4}) f_{44}^-(\boldsymbol{\varepsilon}_{\mathcal{P}4}) \qquad (45)$$

with $1 \le f_{44}^+(\boldsymbol{\varepsilon}_{\mathcal{P}4}) \le 0$ and $1 \le f_{44}^-(\boldsymbol{\varepsilon}_{\mathcal{P}4}) \le 0$. The variables and pa-
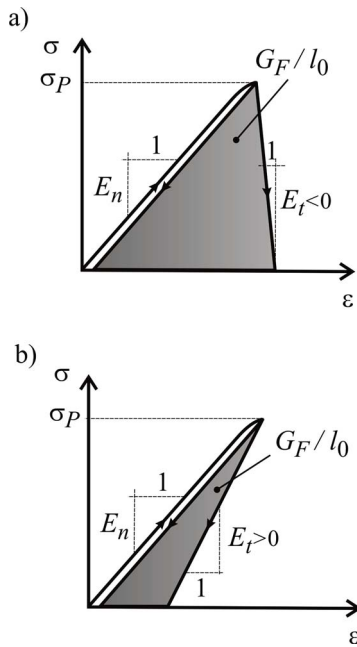
Fig. 4 Mean slope E_t of the post-peak softening curve

rameters in Eq. (45) have meaning similar to the case of mode II.

The formulation presented so far is based on the assumption that the strain modes are substantially independent. As it will be shown in the companion paper [45], even if it is possible to closely reproduce with this assumption the uniaxial behavior of the composite, the simulation of shear versus normal stress strength envelopes is not accurate. A mild interaction between modes significantly improves the fitting of these envelopes and enhances the overall predictive capability of the model. A detailed discussion of this interaction will appear in the subsequent companion paper.

Fracture Mechanics Aspects. Based on the data from the literature, it is impossible to identify the equilibrium post-peak softening curve because in all the tests either the machine stiffness was too low or the specimen size too large to keep the response stable (Sec. 13.2 in [5]). Nevertheless, the mean slope of the post-peak softening curve, or the area under it, can be identified from the value of fracture energy G_F and the material characteristic length l_0 representing roughly the FPZ width, which in turn is approximately equal to the minimum possible spacing h of parallel cracks or the crack band width in the crack band model.

The crack band width can be roughly estimated from visual observations of fracture and typically equals 1.5 to 2 times the material inhomogeneity size (such as spacing of the weave of reinforcing fabric, spacing of fiber strands, or of lamina, etc.). G_F can be most easily determined from size effect tests [16,46], as shown in [9,11]. Since $\sigma_p/E_n + \sigma_p/E_t = G_f/l_0$ = area under the post-peak softening curve and the elastic unloading curve of slope E_t emanating from the peak stress point (Fig. 4). If this curve is assumed to be linear, its slope can be calculated as

$$E_t = -\left(\frac{G_f}{l_0\sigma_p} - \frac{1}{E_n}\right)^{-1} \tag{46}$$

provided that both G_f and l_0 are known; here σ_p=peak stress across the fracture plane, and E_n pertains to stress across the expected crack plane; E_t can be positive or negative, and for a vertical drop it is ∞. An equation analogous to (46) is used in the crack band model (Sec. 13.2 in [5]).

A more detailed discussion of fracture simulation with the present model is beyond the scope of this paper and is planned for subsequent study.

Closing Comment. The spectral stiffness microplane model developed here has several attractive features that need to be translated into a computational algorithm and verified by comparison. This is pursued in the second part of this study, which follows.

References

[1] Rosen, B. W., 1964, "Tensile Failure of Fibrous Composites," AIAA J., **2**, pp. 1985–1991.

[2] Rosen, B. W., 1965, "Mechanics of Composite Strengthening," *Fiber Composite Materials*, ASM, Metals Park, Ohio, Chap. 3.

[3] Adams, D. F., and Doner, D. R., 1967, "Transverse Normal Loading of a Unidirectional Composite," J. Compos. Mater., **1**, pp. 152–164.

[4] Adams, D. F., and Doner, D. R., 1967, "Longitudinal Shear Loading of a Unidirectional Composite," J. Compos. Mater., **1**(1), pp. 4–17.

[5] Bažant, Z. P., and Cedolin, L., 2003, *Stability of Structures: Elastic, Inelastic, Fracture and Damage Theories*, 2nd ed., Dover Publications, New York.

[6] *Engineering Mechanics of Composite Materials*, 1994, I. M. Daniel, and O. Ishai, eds., Oxford University Press, New York.

[7] *Composite Engineering Handbook*, 1997, P. K. Mallik, ed., Marcel Dekker, New York.

[8] Tsai, S. W., and Wu, E. M., 1972, "A General Theory of Strength for Anisotropic Materials," J. Compos. Mater., **5**, pp. 58–80.

[9] Bažant, Z. P., Daniel, I. M., and Li, Z., 1996, "Size Effect and Fracture Characteristics of Composite Laminates," ASME J. Eng. Mater. Technol. **118**(3), pp. 317–324.

[10] Bažant, Z. P., Kim, J.-J. H., Kim, D., I. M., Becq-Giraudon, E., and Zi, G., 1999, "Size Effect on Compression Strength of Fiber Composites Failing by Kink Band Propagation," Int. J. Fract., **95**, pp. 103–141.

[11] Bažant, Z. P., Zhou, Y., Zi, G., and Daniel, I. M., 2003, "Size Effect and Asymptotic Matching Analysis of Fracture of Closed-Cell Polymeric Foam," Int. J. Solids Struct., **40**, pp. 7197–7217.

[12] Bažant, Z. P., Zhou, Y., Novák, D., and Daniel, I. M., 2004, "Size Effect on Flexural Strength of Fiber Composite Laminate," ASME J. Eng. Mater. Technol., **126**(1), pp. 29–37.

[13] Bažant, Z. P., Zhou, Y., Daniel, I. M., Caner, F. C., and Yu, Q., 2006, "Size Effect on Strength of Laminate-Foam Sandwich Plates," ASME J. Eng. Mater. Technol., **128**(3), pp. 366–374.

[14] Bayldon, J. M., Bažant, Z. P., Daniel, I. M., and Yu, Q., 2006, "Size Effect on Compressive Strength of Sandwich Panels With Fracture of Woven Laminate Facesheet," ASME J. Eng. Mater. Technol., **128**, pp. 169–174.

[15] Zi, G., and Bažant, Z. P., 2003, "Eigenvalue Method for Computing Size Effect of Cohesive Cracks With Residual Stress, With Application to Kink Bands in Composites," Int. J. Eng. Sci., **41**(13-14), pp. 1519–1534.

[16] Bažant, Z. P., 2002, *Scaling of Structural Strength*, 2nd ed., Elsevier, London.

[17] Bažant, Z. P., 2004, "Scaling Theory for Quasibrittle Structural Failure," Proc. Natl. Acad. Sci. U.S.A., **101**(37), pp. 14000–14007.

[18] Taylor, G. I., 1938, "Plastic Strain in Metals," J. Inst. Met., **62**, pp. 307–324.

[19] Batdorf, S. B., and Budiansky, B., 1949, "A Mathematical Theory of Plasticity Based on the Concept of Slip," Nat. Advisory Committee for Aeronautics, Washington, D.C., Technical Note No. 1871.

[20] Bažant, Z. P., and Oh, B.-H., 1983, "Microplane Model for Fracture Analysis of Concrete Structures," *Symp. on the Interaction of Non-Nuclear Munitions With Structures*, U.S. Air Force Academy, Colorado Springs, CO, pp. 49–53.

[21] Bažant, Z. P., and Oh, B.-H., 1985, "Microplane Model for Progressive Fracture of Concrete and Rock," J. Eng. Mech., **111**, pp. 559–582.

[22] Bažant, Z. P., Caner, F. C., Carol, I., Adley, M. D., and Akers, S. A., 2000, "Microplane Model M4 for Concrete: I. Formulation With Work-Conjugate Deviatoric Stress," J. Eng. Mech., **126**(9), pp. 944–953.

[23] Bažant, Z. P., Adley, M. D., Carol, I., Jirásek, M., Akers, S. A., Rohani, B., Cargile, J. D., and Caner, F. C., 2000b, "Large-Strain Generalization of Microplane Model for Concrete and Application," J. Eng. Mech., **126**(9), pp. 971–980.

[24] Bažant, Z. P., and Prat, P. C., 1988, "Microplane Model for Brittle Plastic Material: I. Theory," J. Eng. Mech. **114**, pp. 1672–1688.

[25] Bažant, Z. P., Xiang, Y., and Prat, P. C., 1996, "Microplane Model for Concrete. I. Stress-Strain Boundaries and Finite Strain," J. Eng. Mech. **122**(3), pp. 245–254 1996 (with Errata, **123**(3), p. 411).

[26] Caner, F. C., and Bažant, Z. P., 2000, "Microplane Model M4 for Concrete. II: Algorithm and Calibration," J. Eng. Mech., **126**(9), pp. 954–961.

[27] Bažant, Z. P., and Di Luzio, G., 2004, "Nonlocal Microplane Model With Strain-Softening Yield Limits," Int. J. Solids Struct., **41**, pp. 7209–7240.

[28] Bažant, Z. P., and Caner, F. C., 2005, "Microplane Model M5 With Kinematic and Static Constraints for Concrete Fracture and Anelasticity. I: Theory," J. Eng. Mech., **130**(1), pp. 31–40.

[29] Bažant, Z. P., and Caner, F. C., 2005, "Microplane Model M5 With Kinematic and Static Constraints for Concrete Fracture and Anelasticity. II: Computation," J. Eng. Mech., **130**(1), pp. 41–47.

[30] Bažant, Z. P., and Zi, G., 2003, "Microplane Constitutive Model for Porous Isotropic Rock," Int. J. Numer. Analyt. Meth. Geomech., **27**, pp. 25–47.

[31] Bažant, Z. P., and Prat, P. C., 1987, "Creep of Anisotropic Clay: New Microplane Model," J. Eng. Mech., **113**(7), pp. 1000–1064.

[32] Brocca, M., and Bažant, Z. P., 2001, "Microplane Finite Element Analysis of Tube-Squash Test Of Concrete With Angle up to 70^0," Int. J. Numer. Methods Eng., **52**, pp. 1165–1188.

[33] Brocca, M., Bažant, Z. P., and Daniel, I. M., 2001, "Microplane Model for Stiff Foams and Finite Element Analysis of Sandwich Failure by Core Indentation," Int. J. Solids Struct., **38**, pp. 8111–8132.

[34] Beghini, A., Bažant, Z. P., Zhou, Y., Gouirand, O., and Caner, F. C., 2004, "Microplane Model M5f for Fiber Reinforced Concrete: Non-Linear Triaxial Behavior, Strength and Softening," J. Eng. Mech., **133**(1), pp. 66–75.

[35] Carol, I., Jirásek, M., and Bažant, Z. P., 2004, "A Framework for Microplane Models at Large Strain, With Application to Hyperelasticity," Int. J. Solids Struct., **41**, pp. 511–557.

[36] Kuhl, E., and Ramm, E., 2000, "Microplane Modelling of Cohesive Frictional Materials," Eur. J. Mech. A/Solids, **19**, pp. 121–149.

[37] Leukart, M., and Ramm, E., 2006, "Identification and Interpretation of Microplane Material Laws," J. Eng. Mech., **132**(3), pp. 295–305.

[38] Elbing, K., 1994, *Foundations of Anisotropy for Exploration Seismics*, Pergamon Press, Oxford.

[39] Thomson, W., 1878, "Mathematical Theory of Elasticity," *Encyclopedia Britannica*, , Vol. 7, pp. 819–825.

[40] Rychlewski, J., 1995, "Unconventional Approach to Linear Elasticity," Arch. Mech., **47**, pp. 149–171.

[41] Theocaris, P. S., and Sokolis, D. P., 1998, "Spectral Decomposition of the Compliance Tensor for Anisotropic Plates," J. Elast., **51**, pp. 89–103.

[42] Theocaris, P. S., and Sokolis, D. P., 1999, "Spectral Decomposition of the Linear Elastic Tensor for Monoclinic Symmetry," Acta Crystallogr., Sect. A: Found. Crystallogr., **A55**, pp. 635–647.

[43] Theocaris, P. S., and Sokolis, D. P., 2000, "Spectral Decomposition of the Compliance Fourth-Rank Tensor for Orthotropic Materials," Arch. Appl. Mech., **70**, pp. 289–306.

[44] Bažant, Z. P., and Kim, J.-K., 1986, "Creep of Anisotropic Clay: Microplane Model," J. Geotech. Engrg., **112**, pp. 458–475.

[45] Beghini, A., Cusatis, G., and Bažant, Z. P., 2007, "Spectral Stiffness Microplane Model for Quasibrittle Composite Laminates—Part II: Calibration and Validation," ASME J. Appl. Mech., **75**, p. 021010.

[46] Bažant, Z. P., and Planas, J., 1998, *Fracture and Size Effect in Concrete and Other Quasibrittle Materials*, CRC Press, Boca Raton, FL.

Alessandro Beghini

Engineer
Skidmore, Owings and Merrill LLP,
224 South Michigan Avenue,
Chicago, IL 60604
e-mail: alessandro.beghini@som.com

Gianluca Cusatis

Assistant Professor
Civil Engineering Department,
Rensselaer Polytechnic Institute,
110 8th Street,
Troy, NY 12180
e-mail: cusatg@rpi.edu

Zdeněk P. Bažant[1]

Walter P. Murphy Professor and
McCormick School Professor
of Civil Engineering and Materials Science,
CEE Department,
Northwestern University,
2145 Sheridan Road,
Evanston, IL 60208
e-mail: z-bazant@northwestern.edu

Spectral Stiffness Microplane Model for Quasibrittle Composite Laminates—Part II: Calibration and Validation

The spectral stiffness microplane (SSM) model developed in the preceding Part I of this study is verified by comparisons with experimental data for uniaxial and biaxial tests of unidirectional and multidirectional laminates. The model is calibrated by simulating the experimental data on failure stress envelopes analyzed in the recent so-called "World Wide Failure Exercise," in which various existing theories were compared. The present theory fits the experiments as well as the theories that were best in the exercise. In addition, it can simulate the post-peak softening behavior and fracture, which is important for evaluating the energy-dissipation capability of composite laminate structures. The post-peak softening behavior and fracture are simulated by means of the crack band approach which involves a material characteristic length. [DOI: 10.1115/1.2744037]

Keywords: fiber composites, laminates, spectral methods, microplane model, fracture energy, crack band model, damage, failure criteria

Introduction

In Part I of this study [1], a new three-dimensional constitutive model for transversely isotropic (unidirectional) composite laminates has been proposed in the framework of a kinematically constrained spectral stiffness microplane (SSM) model [2]. The formulation exploits the spectral decomposition of the orthotropic stiffness matrix to decompose the strain tensor into four orthogonal strain modes. Strain Modes I and III govern the transverse behavior (which is matrix dominated), Mode II governs the longitudinal behavior (which is fiber dominated), and Mode IV governs the behavior in pure shear. This mode decomposition is a generalization of the deviatoric-volumetric split already adopted in the formulation of microplane models for isotropic materials [3,2]. As it will be seen, in the elastic regime, the four strain modes can be considered to be uncoupled, whereas in the inelastic regime a certain degree of coupling is necessary to achieve good fits of the experimental results.

In the present Part II, the model will be calibrated and validated by comparing numerical results to published experimental data found for typical uniaxial and biaxial tests. Simulations of the behavior of unidirectional and multidirectional carbon–epoxy laminates (AS4 3501-6) will be compared with the experimental data reported in Refs. [4,5] (and references therein). This collection of data was used in the "World Wide Failure Exercise" [6–8], for the purpose of comparing the accuracy of several failure criteria for laminates. Among them, the Tsai–Wu criterion [9] performed the best.

The literature, unfortunately, does not include, for one and the same laminate, a complete set of test data for both the multiaxial failure envelopes and the stress-strain behavior, not even the uniaxial behavior. Therefore, the failure envelopes from other kinds of laminates in Ref. [5] will be scaled, in a proper way, to deduce the likely form of the missing experimental curves for the carbon–epoxy laminates studied here.

The calibrated model will subsequently be used to predict the behavior of multidirectional laminates. Only short-time loading, for which creep is unimportant, and loading rates low enough for dynamic wave propagation effects to be absent, will be considered. All the definitions and notations from Part I will be retained.

Elastic Behavior of Unidirectional Laminates

The elastic behavior of unidirectional carbon–epoxy laminates depends on the elastic properties of the epoxy matrix, and the elastic properties of the fibers. Micromechanical models might be used to get approximate values of the elastic moduli of the laminates based on the experimental data for their components. However, it is preferable to deduce these moduli from the experimental data measured for the given laminate. The experimental elastic properties for carbon/epoxy AS4 3501-6 reported in Ref. [4] are: $E_{33} = 126$ GPa, $E_{11} = 11$ GPa, $\nu_{12} = 0.4$, $\nu_{31} = 0.28$, and $G_{13} = 6.6$ GPa, where $E_{33} =$ longitudinal modulus (in the fiber direction); $E_{11} =$ transverse modulus (in the direction orthogonal to the fibers); $\nu_{12} = \nu_{21} =$ transverse Poisson ratio; ν_{31} $(=\nu_{32}) =$ major Poisson ratio; and G_{13} $(=G_{23}) =$ in-plane shear modulus. Note that the longitudinal modulus E_{33} is actually a secant modulus because the elastic uniaxial stress-strain curve shows (Fig.2) a stiffening behavior due to straightening of the fibers in tension. In absence of more precise experimental data, the same elastic modulus is also assumed to govern the elastic behavior for compression in the longitudinal direction.

The elastic moduli at the microplane level are easy to identify because they equal the eigenvalues of the stiffness matrix [1] associated with the elastic parameters introduced previously, which are: $\lambda_1 = 7.9$ GPa, $\lambda_2 = 145.4$ GPa, $\lambda_3 = 18.2$ GPa, and $\lambda_4 = 13.2$ GPa. The microplane elastic stiffness relevant to strain Mode II (λ_2) is significantly larger than the others (λ_1, λ_3, and λ_4). This confirms that strain Mode II is the mode governing the laminate behavior for loading in fiber direction.
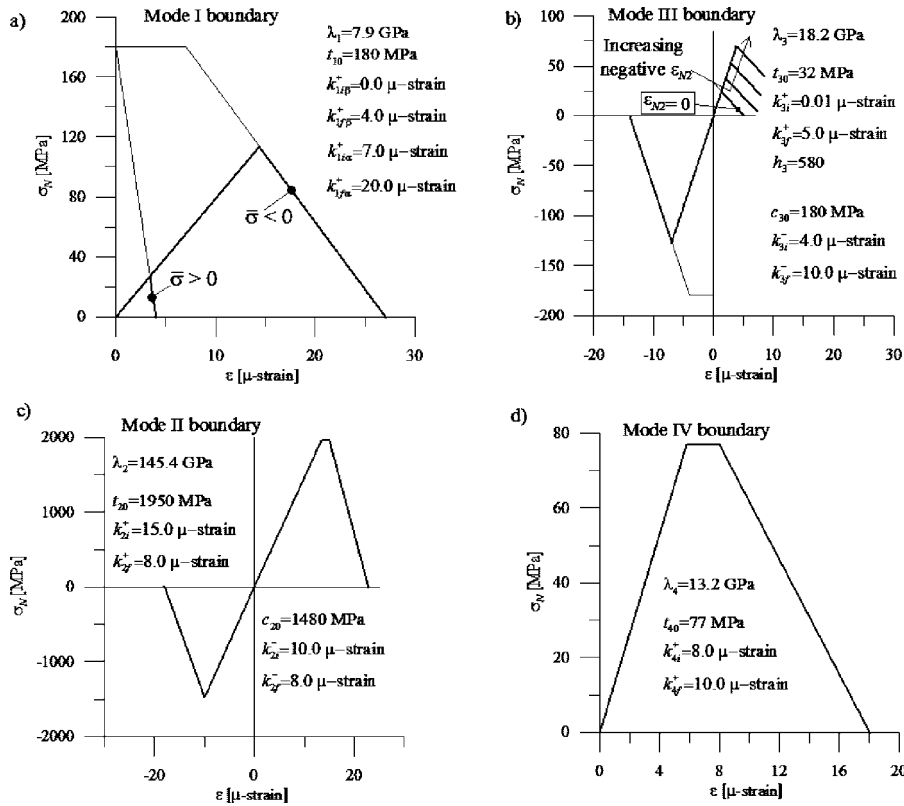
Fig. 1 Stress-strain boundary for the microplane normal component of: (*a*) Mode I; (*b*) Mode III; (*c*) Mode II; and (*d*) Mode IV

Uniaxial Stress-Strain Curves of Unidirectional Laminates

For the uniaxial case, the calibration procedure consists of two steps. First the experimental stress-strain curves are matched in the prepeak region. The post-peak softening parameters are adjusted to match the fracture energy, for which the width of the localization band h [10], representing a material characteristic length, is also needed. In theory, the value of h must be obtained from the fracture energy measured a priori by fracture tests. However, since no data are available, an educated guess based on the size of the inhomogeneities is the only option left. We consider the localization band width of $h=2$ mm (for specimens of length $L=100$ mm) and we assume the same band width for fracture, compression failure, and shear failure. Doubtless, this assumption is crude and, in general, different band widths may be expected to be associated with different phenomena. Nevertheless, by experience with other materials [11], this assumption seems adequate for finite element simulations, and having only one band width is convenient since the characteristic finite element size is usually made to coincide with this width.

Let us now analyze the laminate behavior under transverse compression and tension. The experimental data available for these loading conditions are the peak stress in tension and compression ($F_{1t}=48$ MPa, $F_{1c}=-200$ MPa), peak strains in tension and compression ($\varepsilon_{1t}=4.36$ μstrain, $\varepsilon_{1c}=-20$ μstrain), stress-strain curve in compression up to the peak, and the interlaminar fracture energy ($G_F^t=220$ J/m^2) identified from a double cantilever beam specimen [4]. The interlaminar fracture energy can be assumed to be a good approximation of the transverse fracture energy. This assumption is supported by Daniel and Lee's [12] measurements of the progressive damage in $[0_n/90_m]_s$ coupons of graphite–epoxy, in which the 90 deg layers fractured and the 0 deg layers remained elastic. From these experiments, it is pos-

sible to deduce the fracture energy in transverse direction, and its value turns out to be very close to the aforementioned value of the interlaminar fracture energy.

The transverse behavior is governed by Mode I and Mode III [1]. The identified microplane parameters that fit the aforementioned macroscopic properties (for $h=2$ mm) are $t_{10}=c_{10}=180.0$ MPa, $k_{1i\alpha}^+=k_{1i\alpha}^-=7.0\times10^{-6}$, $k_{1f\alpha}^+=k_{1f\alpha}^-=20.0\times10^{-6}$, $k_{1i\beta}^+=k_{1i\beta}^-=0.0$, $k_{1f\beta}^+=k_{1f\beta}^-=4.0\times10^{-6}$, $t_{30}=32.0$ MPa, $k_{3i}^+=0.01\times10^{-6}$, $k_{3f}^+=5.0\times10^{-6}$, $c_{30}=180.0$ MPa, $k_{3i}^-=4.0\times10^{-6}$, $k_{3f}^-=10.0\times10^{-6}$n, $s_{10}=77$ MPa, and $s_{30}=90$ MPa.

Figures 1(*a*) and 1(*b*) show the stress-strain boundaries of the microplane normal component for Mode I (tension) and Mode III (tension and compression) according to the foregoing parameters.

The parameters of Mode I compressive boundary are assumed to be equal to those of the tensile boundary. This assumption is necessary because strain Mode I is a quasideviatoric mode in the plane of isotropy exhibiting both tension and compression at the microplane level, regardless of the sign of the applied macroscopic transverse stress. The macroscopic behavior is, of course, not symmetric and the tensile strength is much smaller than the compressive strength. To take into account this asymmetry, the Mode I boundary has been made to depend upon the mean stress $\bar{\sigma}$ in the plane of isotropy (Fig. 1(*a*)); $\bar{\sigma}$ provides a measure of confinement of the fiber and permits distinguishing between Mode I strains associated with the macroscopic transverse tension ($\bar{\sigma}>0$) and with the macroscopic transverse compression ($\bar{\sigma}<0$).

Because of the lack of data in the post-peak portion of the compressive stress-strain curve, parameters $k_{1i\alpha}^-$, $k_{1i\beta}^-$, $k_{1i\alpha}^-$, $k_{1i\beta}^-$, k_{3i}^-, and k_{3f}^- cannot be properly calibrated. The reported values are obtained by matching only the pre-peak nonlinearity (Fig. 2(*d*)). The identification of these parameters is, of course, less than satisfactory and further studies are needed.

Figures 2(*c*) and 2(*d*) compares the experimental data (points)
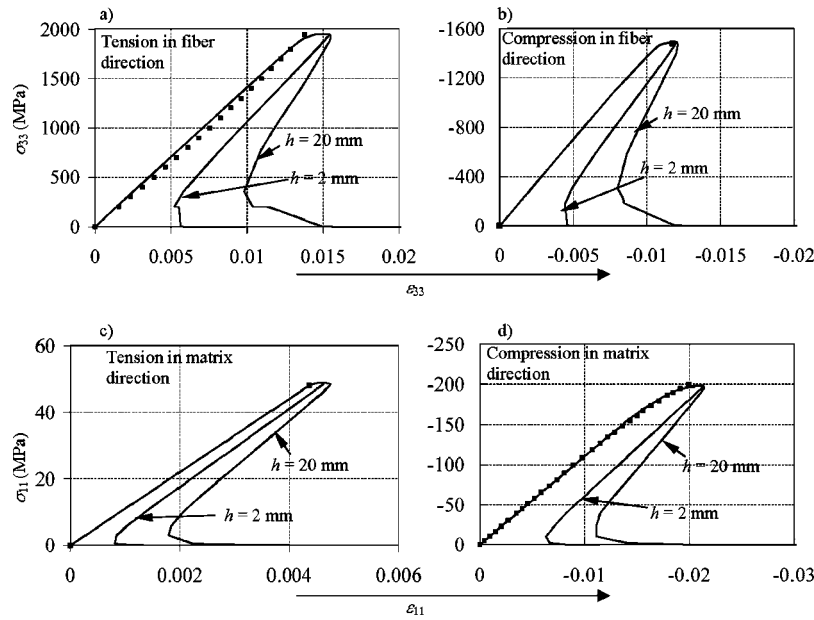
Fig. 2 Uniaxial stress-strain curves. Comparison between numerical simulations (solid line) and experimental results (points) from Soden et al. [4,5]) for: (*a*) tension in fiber direction; (*b*) compression in fiber direction; (*c*) tension in transverse direction; and (*d*) compression in transverse direction

with the calculated stress-strain curves (solid lines) for $h=2$ mm. The curves clearly exhibit snapback [13], which explains why, in experiments, the failure of laminates is dynamic and sudden, making the post-peak equilibrium curve unobservable.

For comparison, Figs. 2(*c*) and 2(*d*) also show the stress-strain curves obtained with the aforementioned parameters and $h=20$ mm. Of course in this case the fracture energy turns out to be ten times larger than the experimental value.

As far as the uniaxial behavior in the fiber direction is concerned, the available experimental data consist of the peak stress in tension and compression ($F_{3t}=1950$ MPa, $F_{3c}=1480$ MPa), peak strain in tension and compression ($\varepsilon_{3t}=13.8\times10^{-6}$, $\varepsilon_{3c}=-11.75\times10^{-6}$), and the stress-strain curve in tension up to the peak. Data are available on the post-peak for neither tension nor compression. The peak stress in tension is matched by setting $t_{20}=1950$ MPa and $k_{2i0}^{+}=15.0\times10^{-6}$.

The fitting of the compressive peak stress is slightly more complicated because high compressive stress in the direction of the fibers generates Mode III tensile stresses on those microplanes whose normal orientation is close to the transverse direction. These stresses must quickly lead to a splitting-like failure because of the low tensile strength associated with Mode III. The experimental results, however, do not indicate this kind of failure. On the contrary, they show the failure to be triggered by microbuckling of the fibers. Since microbuckling must be associated with Mode II, and not with Mode III, the splitting-like failure must be somehow prevented in these simulations. To this end, the peak of Mode III normal boundary is radially scaled up as a function of the negative Mode II strain (Fig. 1(*b*)). The radial scaling is formulated through functions h_3^{+} abd k_{3i}^{+} presented in Part I [1]. The identified microplane parameters are $c_{20}=1480$ MPa, $k_{2i}^{-}=10.0\times10^{-6}$, $s_{20}=77$ MPa, and $h_3=580$ (h_3 governs the radial scaling of the boundary associated with Mode III as a function of the negative normal strain of Mode II).

In absence of any information about the post-peak part of the stress-strain curves, it is impossible to identify from such curves parameters k_{2f}^{+} and k_{2f}^{-} that define the post-peak slope of the normal boundary, associated with Mode II for tension and compression, respectively. We assume $k_{2f}^{+}=k_{2f}^{-}=8.0\times10^{-6}$. Figure 1(*c*)

shows the compressive and tensile boundaries for Mode II used in the numerical simulations, and Figs. 2(*a*) and 2(*b*) show the comparison between the experimental data (points) and the numerical simulations (solid lines).

To conclude the analysis of uniaxial behavior of the unidirectional laminate, we need to analyze the response under macroscopic in-plane shear stress. This response is governed solely by the strain Mode IV [1]. The optimization of the relevant microplane model parameters can be done by fitting the stress-strain curve, which, however, was available only up to the peak. The best fits, shown in Fig. 3, have been obtained by setting $t_{40}=c_{40}=77.0$ MPa, $k_{4i}^{+}=k_{4i}^{-}=8.9\times10^{-6}$. We also assumed that $k_{4f0}^{+}=k_{4f0}^{-}=10.0\times10^{-6}$. These last two parameters govern the undocumented post-peak segment of the curve.

Biaxial Failure Envelope of Unidirectional Laminates Without Mode Interaction

Let us now analyze failure of the carbon–epoxy unidirectional laminates under biaxial loading. Following the "World Wide Failure Exercise," we consider three different biaxial loading conditions: (1) transverse and in-plane shear loadings; (2) longitudinal
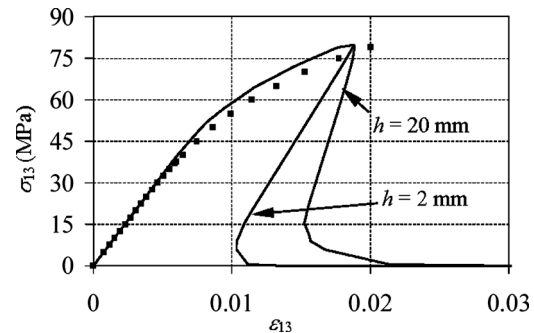
Fig. 3 Comparison between numerical simulations (solid line) and experimental results (points) from Soden et al. [4,5] for shear loading
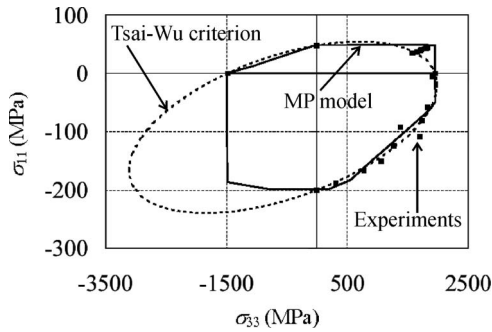
Fig. 4 Comparison between numerical simulations (solid line), Tsai–Wu criterion (dashed line), and experimental results (points) from Soden et al. [4,5] for multiaxial failure envelope with: (a) no interaction of modes; and (b) with interaction

and in-plane shear loadings; and (3) longitudinal and transverse loadings. Unfortunately, the associated failure envelopes available in the literature and reported in Ref. [5] were measured on three different kinds of laminates. To check the ability of the model to predict, with the same set of parameters, the response of unidirectional carbon–epoxy laminates under all the three aforementioned loading conditions, the biaxial failure envelopes are assumed to be scaled radially according to the uniaxial strengths.

Figure 4 compares the experimental data (points), the microplane model prediction (solid line), and the prediction of the Tsai–Wu criterion (dashed line), which performed the best during the "World Wide Failure Exercise."

In the first quadrant (tension–tension), the microplane model, and the Tsai–Wu criterion agree quite well for matrix-dominated failures (low and moderate longitudinal stresses). For high longitudinal stresses, the Tsai–Wu criterion is more conservative than the microplane model. Unfortunately, the experimental results do not help to validate one theory more than the other because they are quite scattered and lie in the middle between the two predicted curves. In the second quadrant (longitudinal tension—transverse compression) the agreement between the two theories and the ex-

perimental results is excellent. The same good agreement can be seen in the fourth quadrant (transverse tension—longitudinal compression).

An important discrepancy between the microplane model and the Tsai–Wu criterion is in the third quadrant (compression–compression), in which the Tsai–Wu criterion predicts a much larger strength than the microplane model. Unfortunately, there are no experimental data available to check which theory is correct.

Figure 5(a) shows the failure envelopes for transverse and in-plane shear loading. In this case, the microplane model prediction resembles the maximum stress criterion and is poor. The prediction of the Tsai–Wu criterion is somewhat better but it does not predict the skew character of the envelopes, which shows that the shear strength in the presence of transverse compression is higher, as expected. A similar picture arises from analyzing the failure envelope for longitudinal and in-plane shear loading. Without mode interaction (Fig. 5(c)), the prediction of the microplane model cannot be fully accurate, but still is reasonable.

Formulation With Mode Interaction

Performance of the microplane model can be significantly enhanced even if only a limited interaction between the strain modes is introduced. In Fig. 5(a), the vertical portions of the envelope are associated with failures in the matrix and fiber-matrix interface. Consequently they are governed by Modes I and III. On the contrary, the horizontal portion of the envelope is associated with pure shear failure and is governed by Mode IV. Therefore, to match the experimental data, one needs to introduce interaction between Modes I, III and Mode IV. This can be achieved by formulating the following interaction functions

$$f_{14}^+(\boldsymbol{\epsilon}_\mathcal{P}) = f_{14}^-(\boldsymbol{\epsilon}_\mathcal{P}) = g_{14}(\boldsymbol{\epsilon}_\mathcal{P}) = f_{34}^+(\boldsymbol{\epsilon}_\mathcal{P}) = f_{34}^-(\boldsymbol{\epsilon}_\mathcal{P}) = g_{34}(\boldsymbol{\epsilon}_\mathcal{P}) = 1 + \tau_4\varepsilon_4 \tag{1}$$

$$f_{41}^+(\boldsymbol{\epsilon}_\mathcal{P}) = f_{41}^-(\boldsymbol{\epsilon}_\mathcal{P}) = g_{41}(\boldsymbol{\epsilon}_\mathcal{P}) = \langle 1 - \text{sign}(\varepsilon_{N3})|\varepsilon_{N1}|/\tau_1\rangle \tag{2}$$

where $\tau_4 = \tau_4^-$ for $\bar{\sigma} < 0$, and $\tau_4 = \tau_4^+$ for $\bar{\sigma} > 0$.

The best fit of the failure envelope in Fig. 5(b) can be obtained upon setting $\tau_4^+ = 0.1$, $\tau_4^- = 0.02$, and $\tau_1^+ = 0.002$. The microplane
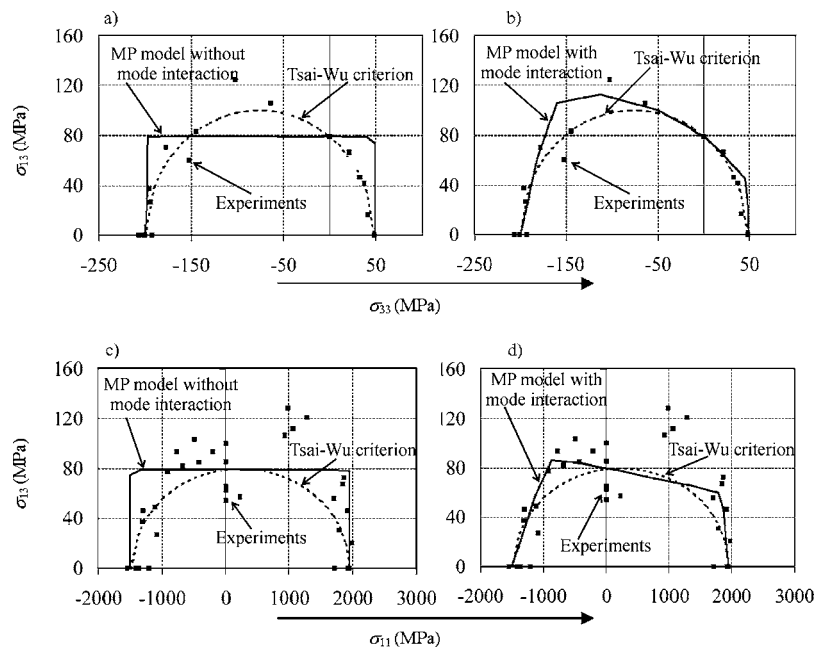
Fig. 5 Comparison between numerical simulations (solid line) and experimental results (points) from Soden et al. [4,5] for uniaxial loading in fiber direction
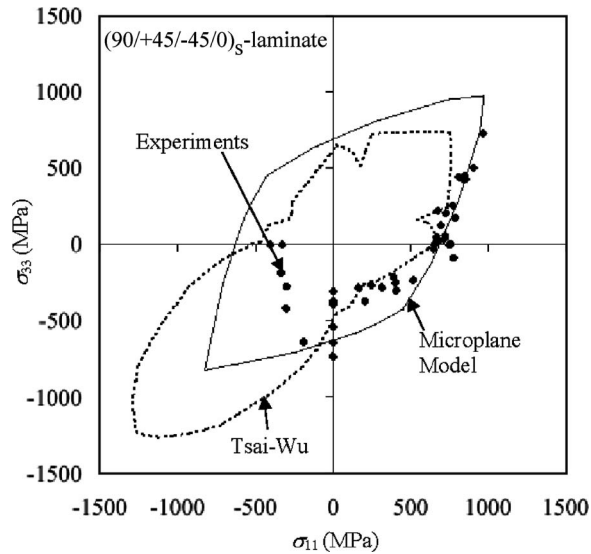
Fig. 6 Comparison between numerical simulations (solid line), Tsai–Wu criterion (dashed line), and experimental results (points) from Soden et al. [4,5] for multiaxial failure envelope with: (*a*) no interaction of modes; and (*b*) with interaction

model prediction is now in good agreement with the experimental data and is more accurate than the prediction of Tsai–Wu criterion.

The microplane prediction of the failure envelope in Fig. 5(*c*) can also be improved through mode interaction. In this case, the relevant modes are Mode II (behavior in fiber direction) and Mode IV (pure shear), and so it is these two that should be linked. The effect of Mode IV on Mode II is formulated in the same manner as the effect of Mode IV on Modes I and III

$$f_{24}^+(\boldsymbol{\epsilon}_{\mathcal{P}}) = f_{24}^-(\boldsymbol{\epsilon}_{\mathcal{P}}) = g_{24}(\boldsymbol{\epsilon}_{\mathcal{P}}) = 1 + \tau_4 \varepsilon_4 \tag{3}$$

In addition, the effect of Mode II on Mode IV can be formulated as follows

$$f_{42}^+(\boldsymbol{\epsilon}_{\mathcal{P}}) = f_{42}^-(\boldsymbol{\epsilon}_{\mathcal{P}}) = g_{42}(\boldsymbol{\epsilon}_{\mathcal{P}}) = \langle 1 - \tau_2 \varepsilon_{N2} \rangle \tag{4}$$

where $\langle x \rangle = \max(x,0)$. The best fit of the failure envelope, shown in Fig. 5(*d*), is obtained by setting $\tau_2 = 50$.

Analysis of Multidirectional Laminates

A widely used laminate layup is $(90/+45/-45/0)_S$, which is quasi-isotropic. Several authors studied the AS4/3501-6 carbon–epoxy quasi-isotropic laminate. The relevant data and reference to the original publications can be found in Ref. [5]. The tests were carried out by subjecting tubular specimens to pressure and axial loads. To avoid spurious ruptures at the connections with the loading platens, the specimens had been reinforced at the ends. Because of this end constraint, it is reasonable to assume that the specimens could not have experienced any torsional rotation. This means that the plies were subjected only to longitudinal and circumferential (hoop) strains, and that the shear strains vanished in all the plies. This, in turn, implies the appearance of shear stresses in the +45 and −45 plies. These stresses are important and, if neglected, lead to a significant underestimation of the laminate strength.

The behavior of this multidirectional laminate is here simulated assuming each ply to be governed by the microplane model for unidirectional laminates (see Part I, [1]) and calibrated in the preceding sections. At this stage, no adjustment to the model parameters is allowed, so that the numerical solution would truly be a prediction. An iterative Newton–Rapson procedure is used to converge to a vanishing out-of-plane normal stress for all plies.

Figure 6 shows a comparison between the experiments (data points), the microplane model prediction (solid line), and the pre-

diction of the Tsai–Wu criterion (dashed line). The microplane model theory agrees very well with the experimental data in the tension-tension quadrant of the envelope. For the tension-compression quadrant, the prediction is less accurate but still satisfactory. However, marked disagreement is found in the compression-compression quadrant, in which both the microplane model and the Tsai–Wu criterion severely overestimate the laminate strength. This shortcoming is, most probably, due to the fact that the microplane calibration for the unidirectional laminate could not rely on any data for the compression-compression quadrant.

Conclusions

1. The spectral decomposition theorem is a powerful tool to analyze generally anisotropic materials. This is the *only* known exact and rigorous approach for the anisotropic generalization of the microplane model.
2. The mechanical behavior of laminate composites can be subdivided into characteristic loading conditions representing the longitudinal tension or compression, transverse tension or compression, and shear, most of which are dominated by one spectral mode, and none by more than two spectral modes.
3. Interaction of modes, which it has been possible to avoid, with minor exceptions, in the previous microplane formulations, helps to achieve better fit of some experimental multiaxial failure envelopes of laminates. Even if this interaction is not dominant, its neglect always causes a single mode to reach its strength limit before the others, which impairs the fits of some multiaxial data.
4. The present SSM model describes well the experimentally observed behavior of fiber composites, not only for uniaxial stress-strain curves, but also for multiaxial failure envelopes. The fitting capabilities for multiaxial failure envelopes are superior to the Tsai–Wu criterion, which has so far been considered as overall the best model for laminates.
5. The main advantage of the SSM model is that one and the same model can simulate the orthotropic stiffness, failure envelopes, and the post-peak behavior, which include strain-softening damage and fracture mechanics aspects. This further implies that the SSM model must be able to automatically predict the energetic size effect.
6. The material parameters of the SSM model can be identified from experiments by a sequential procedure. Post-peak data are needed to identify the parameters governing the softening, and an estimate can be based on the width of the localization band taken equal to the inhomogeneity size.
7. The experimental failure envelopes can be represented by the present model as well or better than with the existing failure criteria, including Tsai–Wu.
8. Although, due to stability limitations of current testing, post-peak measurements are missing, the post-peak softening curve can be approximately inferred from the notched fracture energy test and an estimate of the fracture process zone width.
9. The SSM model can be implemented as a material subroutine in finite element codes, either implicit or explicit. From experience with microplane models for concrete (used in the commercial code ATENA) the kinematically constrained formulation is known to be very stable in finite element analysis.

Acknowledgment

appointment and graduate research assistantship, respectively, from these sources.

Appendix: Calibration Procedure

The procedure of sequential identification of microplane model parameters may be summarized as follows:

(1) Identify elastic parameters λ_1, λ_2, λ_3, and λ_4 (eigenvalues of the stiffness matrix) on the basis of the measured elastic properties (see Eqs. (28)–(31) in Ref. [1]).

(2) Identify parameters t_{20}, c_{20}, and s_{20} on the basis of the uniaxial tensile, compressive, and shear strength in the fiber direction.

(3) Identify parameters k_{2i}^+, k_{2f}^+, k_{2i}^-, k_{2f}^- according to the post-peak softening behavior of the unidirectional lamina tested in fiber direction.

(4) Identify parameters t_{10}, c_{10}, s_{10}, t_{30}, c_{30}, and s_{30} on the basis of the uniaxial tensile, compressive, and shear strength in the direction transverse to the fiber.

(5) Identify parameters k_{3i}^+, k_{3f}^+, k_{3i}^-, k_{3f}^-, $k_{1i\alpha}^+$, $k_{1i\alpha}^-$, $k_{1f\alpha}^+$, $k_{1f\alpha}^-$, $k_{1i\beta}^+$, $k_{1i\beta}^-$, $k_{1f\beta}^+$, $k_{1f\beta}^-$ according to the post-peak softening behavior of the unidirectional lamina tested in direction transverse to the fiber.

(6) Identify parameters t_{40}, c_{40}, s_{40}, k_{4i}^+, k_{4i}^-, k_{4f}^+, k_{4f}^- according to the in-plane shear strength and post-peak softening characteristics of the unidirectional laminate.

References

[1] Cusatis, G., Beghini, A., and Bažant, Z. P., 2005, "Spectral Stiffness Microplane Model for Quasibrittle Composite Laminates—Part I: Theory," J. Appl. Mech., **75**, p. 021009.

[2] Bažant, Z. P., Caner, F. C., Carol, I., Adley, M. D., and Akers, S. A., 2000, "Microplane Model M4 for Concrete: I. Formulation With Work-Conjugate Deviatoric Stress," J. Eng. Mech., Trans. ASCE, **126**(9), pp. 944–953.

[3] Bažant, Z. P., and Prat, P. C., 1988, "Microplane Model for Brittle Plastic Material: I. Theory," J. Eng. Mech. ASCE, **114**, 1672–1688.

[4] Soden, P. D., Hinton, M. J., and Kaddour, A. S., 1998, "Lamina Properties, Lay-up Configurations and Loading Conditions for a Range of Fiber-Reinforced Composite Laminates," Compos. Sci. Technol., **58**(7), pp. 1011–1022.

[5] Soden, P. D., Hinton, M. J., and Kaddour, A. S., 2002, "Biaxial Test Results for Strength and Deformation of a Range of E-Glass and Carbon Fiber Reinforced Composite Laminates: Failure Exercise Benchmark Data," Compos. Sci. Technol., **62**, pp. 1489–1514.

[6] Hinton, M. J., and Soden, P. D., 1998, "Predicting Failure in Composite Laminates: the Background to the Exercise," Compos. Sci. Technol., **58**, pp. 1001–1010.

[7] Hinton, M. J., Kaddour, A. S., and Soden, P. D., 1998, "Failure Criteria in Fiber Reinforced Polymeric Composite," Compos. Sci. Technol., **58**, pp. 1225–1254.

[8] Hinton, M. J., Kaddour, A. S., and Soden, P. D., 2002, "A Comparison of the Predictive Capabilities of Current Failure Theories for Composite Laminates Judged Against Experimental Evidence," Compos. Sci. Technol., **62**, pp. 1725–1797.

[9] Tsai, S. W., and Wu, E. M., 1972, "A General Theory of Strength for Anisotropic Materials," J. Compos. Mater., **5**, pp. 58–80.

[10] Bažant, Z. P., and Oh, B.-H., 1983, "Crack Band Theory for Fracture of Concrete," Mater. Struct. (Rilem, Paris), **16**, pp. 155–177.

[11] Bažant, Z. P., and Planas, J., 1998, *Fracture and Size Effect in Concrete and Other Quasibrittle Materials*, CRC, Boca Raton, FL.

[12] Daniel, I. M., and Lee, J. W., 1990, "Damage Development in Composite Laminates Under Monotonic Loading," J. Compos. Technol. Res., **12**(2), pp. 98–102.

[13] Bažant, Z. P., and Cedolin, L., 1991, *Stability of Structures: Elastic, Inelastic, Fracture and Damage Theories*, Oxford University Press, New York; republication with updates, 2003, Dover, New York.